A&A 518, L143 (2010)
DOI: 10.1051/0004-6361/201014562

Astronomy & Astrophysics
Special feature

Herschel: the first science highlights

Letter to the Editor

Silicon in the dust formation zone of IRC +10216⋆,⋆⋆

L. Decin[1,2], J. Cernicharo[3], M. J. Barlow[4], P. Royer[1], B. Vandenbussche[1], R. Wesson[4], E. T. Polehampton[5,6], E. De Beck[1], M. Agúndez[3,9], J. A. D. L. Blommaert[1], M. Cohen[8], F. Daniel[3], W. De Meester[1], K. Exter[1], H. Feuchtgruber[10], J. P. Fonfría[7], W. K. Gear[11], J. R. Goicoechea[3], H. L. Gomez[11], M. A. T. Groenewegen[12], P. C. Hargrave[11], R. Huygen[1], P. Imhof[13], R. J. Ivison[14], C. Jean[1], F. Kerschbaum[16], S. J. Leeks[5], T. Lim[5], M. Matsuura[4,17], G. Olofsson[15], T. Posch[16], S. Regibo[1], G. Savini[4], B. Sibthorpe[14], B. M. Swinyard[5], B. Tercero[3], C. Waelkens[1], D. K. Witherick[4], and J. A. Yates[4]

(Affiliations are available in the online edition)

Received 30 March 2010 / Accepted 27 April 2010

ABSTRACT

The interstellar medium is enriched primarily by matter ejected from evolved low and intermediate mass stars. The outflows from these stars create a circumstellar envelope in which a rich gas-phase and dust-nucleation chemistry takes place. We observed the nearest carbon-rich evolved star, IRC +10216, using the PACS (55−210 μm) and SPIRE (194−672 μm) spectrometers on board *Herschel*. We find several tens of lines from SiS and SiO, including lines from the $v = 1$ vibrational level. For SiS these transitions range up to $J = 124-123$, corresponding to energies around 6700 K, while the highest detectable transition is $J = 90-89$ for SiO, which corresponds to an energy around 8400 K. Both species trace the dust formation zone of IRC +10216, and the broad energy ranges involved in their detected transitions permit us to derive the physical properties of the gas and the particular zone in which each species has been formed. This allows us to check the accuracy of chemical thermodynamical equilibrium models and the suggested depletion of SiS and SiO due to accretion onto dust grains.

Key words. techniques: spectroscopic – stars: AGB and post-AGB – stars: carbon – circumstellar matter – stars: mass-loss – stars: individual: IRC +10216

1. Introduction

IRC +10216 (CW Leo) is the brightest non-Solar System object in the sky at 5 μm. It is the nearest ($D \sim 150$ pc, Crosas & Menten 1997) carbon-rich evolved star, and it serves as an archetype for the study of mass loss on the asymptotic giant branch (AGB). The star is losing mass at a rate of $\sim 1-3\times10^{-5}\,M_{\odot}$/yr (Crosas & Menten 1997; Schöier & Olofsson 2000), producing a dense, dusty circumstellar envelope (CSE). To date, more than 60 molecules have been detected in the CSE of IRC +10216 (e.g., Cernicharo et al. 2000; He et al. 2008). Thermodynamic equilibrium and non-equilibrium reactions, photochemical reactions, ion-molecule reactions, and the condensation of dust grains establish the abundance stratifications throughout the envelope. It is likely that IRC +10216 is in an advanced evolutionary stage, marking the transition from an AGB to a planetary nebula (Skinner et al. 1998). A detailed study of its infrared emission spectrum can yield unique information on the thermophysical and chemical structure of the outflow and on the history of mass loss during this important evolutionary phase.

2. Observations and data reduction

Thanks to its high infrared brightness, IRC +10216 is an ideal target for observation with *Herschel* (Pilbratt et al. 2010). PACS and SPIRE spectroscopic observations were obtained in the context of the guaranteed time key programme "Mass-loss of Evolved StarS" (Groenewegen et al., in prep.).

The PACS instrument, its in-orbit performance and calibration, and its scientific capabilities are described in Poglitsch et al. (2010). The PACS spectroscopic observations of IRC +10216 consist of full SED scans between 52 and 210 μm obtained in a 3 × 1 raster, i.e. a pointing on the central object, and two pointings 30″ either side. The observations were performed on 2009 Nov. 12 (OD 182). The position angle was 110 degrees. The instrument mode was a non-standard version of the chop-nod PACS-SED AOT, used with a large chopper throw (6′). The spectral resolving power varies between 1000 and 4500. A description of the observing mode and of the data reduction process can be found in Royer et al. (2010). The only difference with the data reduction of VY CMa as presented in Royer et al. (2010) is that the ground-based calibration was used for IRC +10216. The estimated calibration uncertainty on the line fluxes is 50%.

The SPIRE FTS measures the Fourier transform of the source spectrum across short (SSW, 194−313 μm) and long (SLW, 303−671 μm) wavelength bands simultaneously. The *FWHM* beamwidths of the SSW and SLW arrays vary between 17−19″ and 29−42″ respectively. The source spectrum, including the continuum, is restored by taking the inverse transform of the observed interferogram. The absolute flux calibration uncertainty is 15−20% in the SSW band and 20−30% in the SLW band above 20 cm^{-1} (up to 50% below 20 cm^{-1}). For more details on the SPIRE FTS and its calibration see Griffin et al. (2010) and Swinyard et al. (2010).

⋆ *Herschel* is an ESA space observatory with science instruments provided by European-led Principal Investigator consortia and with important participation from NASA.

⋆⋆ Appendix is only available in electronic form at http://www.aanda.org

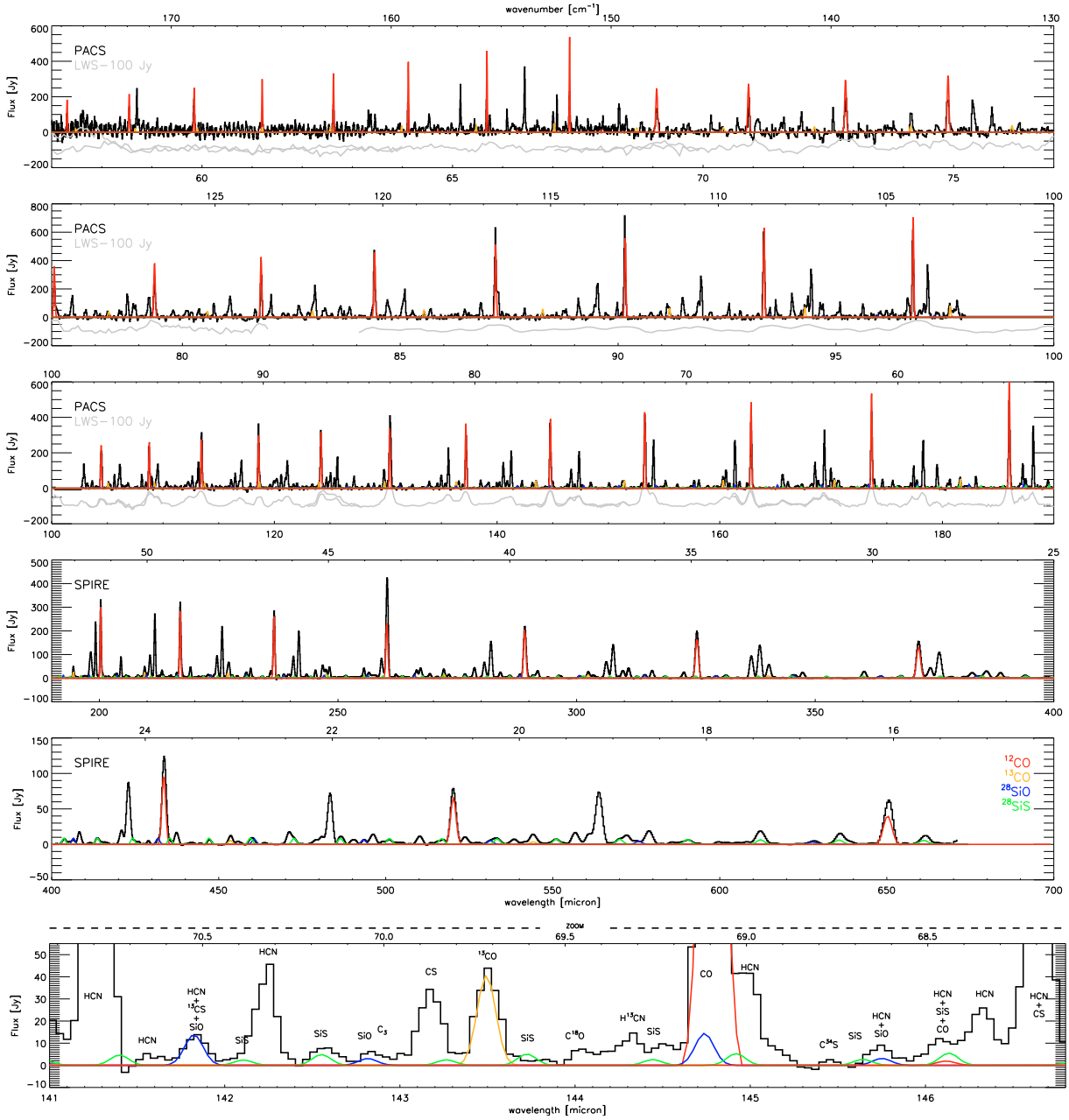

Fig. 1. Continuum-subtracted PACS and SPIRE spectrum of IRC +10216. In the three upper panels, the PACS spectrum of IRC +10216 (black) is compared to the ISO-LWS spectrum (grey, Cernicharo et al. 1996). The fourth and fifth panels show the SPIRE spectrum of IRC +10216 (black). The bottom panel zooms in on the 141−146.8 μm region, where we identified the main molecular features. Theoretical line predictions for ^{12}CO (red), ^{13}CO (orange), ^{28}SiO (blue), and ^{28}SiS (green) using the parameters as given in Table 1 are displayed in all panels.

IRC +10216 was observed with the high-resolution mode of the SPIRE FTS on the 2009 Nov. 19 (OD 189). Twenty repetitions were used, each of which consisted of one forward and one reverse scan of the FTS, with each scan taking 66.6 s. The total on-source integration time was therefore 2664s. The unapodized spectral resolution is 1.4 GHz (0.048 cm^{-1}), and this is 2.1 GHz (0.07 cm^{-1}) after apodization (using extended Norton-Beer function 1.5; Naylor & Tahic 2007).

PACS and SPIRE photometry observations of IRC +10216 are presented in Ladjal et al. (2010).

3. Results

Currently, more than 500 molecular emission lines have been identified in the PACS and SPIRE spectra of IRC +10216 (see Fig. 1), belonging to 10 different molecules and their isotopologues (^{12}CO, ^{13}CO, C^{18}O, H^{12}CN, H^{13}CN, H_2O, NH_3, SiS, SiO, CS, C^{34}S, ^{13}CS, C_3, C_2H, HCl, and H^{37}Cl). The detection of this last molecule is discussed by Cernicharo et al. (2010). In the ISO-LWS spectrum shown in Fig. 1, 57 lines belonging to CO and HCN were identified by Cernicharo et al. (1996). The number of identified lines increases to 280 in the PACS spectrum thanks to its higher spectral resolution. Most of the lines in the PACS and SPIRE spectrum arise from HCN, with the strongest lines from ^{12}CO. HCN is one of the most abundant molecular species in the CSEs of carbon stars (Willacy & Cherchneff 1998) and it is known to show maser action in various vibrational states. The strength of the ^{12}CO lines are diagnostics for the thermophysical structure (see Sect. 3.1). In this paper, we

focus on the silicon-bearing molecules SiS and SiO, two refractory species that are formed in the inner envelope. As soon as the temperature of the gas falls below a certain critical value, the molecules can start to condense and form dust grains.

High-J rotational lines have been detected from both molecules. For SiO, 80 rotational transitions in the ground-state from $J = 11-10$ to $J = 90-89$ ($E_{\rm up} = 8432$ K), and 99 lines from $J = 26-25$ to $J = 124-123$ ($E_{\rm up} = 6678$ K) for SiS are clearly detected. From the detected lines, ~45% of both species is unblended (see Table A.1 in the online Appendix, which also lists the detected ^{12}CO and ^{13}CO lines). The emission lines of higher-J transitions and rotational transitions in the first vibrational state are very weak, but their line contribution can be deduced from the theoretical modelling (see Sect. 3.2, and Table A.1). The line formation region of the highest-J lines of SiO (SiS) is within the first $5\,R_\star$ ($10\,R_\star$), i.e., tracing the recently identified dust formation region (Fonfría et al. 2008).

3.1. Thermophysical structure of the envelope

The large number of optically thick ^{12}CO and optically thin ^{13}CO lines enabled us to perform a tomographical study of the CSE. Properties of the circumstellar gas, such as the kinetic temperature, velocity, and density structure, were determined through a non-local thermodynamic equilibrium (non-LTE) radiative transfer modelling of the ^{12}CO lines. The ^{12}CO lines cover energy levels from $J = 3$ (at 31 K) to $J = 47$ (at 5853 K) and trace the envelope for radii $R < 1 \times 10^{17}$ cm ($R < 2000\,R_\star$). The GASTRoNOoM code was used to calculate the kinetic temperature and velocity structure in the envelope and to solve the non-LTE radiative transfer equations (Decin et al. 2006, 2010). The rate equations were solved for the ground and first excited vibrational state, with $J^{\rm up}_{\rm max} = 60$. The CO line list and collisional rates are discussed in Decin et al. (2010). The terminal velocity was deduced from ground-based observations of low-J ^{12}CO lines (De Beck et al. 2010). The GASTRoNOoM code computes the velocity structure by solving the momentum equation and the temperature structure from the equation expressing the conservation of energy (see Eq. (6) in Decin et al. 2006). However, the resulting temperature was slightly too low beyond $60\,R_\star$ to correctly predict the lower excitation ^{12}CO lines, which mainly reflects uncertainties in the gas-grain collisional heating. Therefore, we opted to use $T(R) \propto R^{-0.5}$ for $R > 60\,R_\star$.

The best-fit model was determined using the log-likelihood function as described in Decin et al. (2007). The derived (circum)stellar parameters are given in Table 1, the deduced thermodynamical structure is displayed in Fig. 2, and the line predictions are shown in Fig. 1. Specifically, we obtained a mass loss rate of $1 \times 10^{-5}\,M_\odot$/yr (with an uncertainty of a factor 2) and a ^{12}CO/^{13}CO ratio of $\sim 30 \pm 5$. The latter is on the lower side of the range of ^{12}C/^{13}C ratios quoted in the literature, going from 20 (Barnes et al. 1977) to 50 (Schöier & Olofsson 2000). The lowest value is obtained from vibra-rotational transitions in the fundamental band of CO, and higher values are often obtained from low-excitation CO or CS lines. The accuracy of isotopologue ratios obtained from low-excitation rotational transitions is often limited by the uncertain effect of photodissociation by interstellar UV photons and chemical fractionation (e.g., Mamon et al. 1988), effects that are not hampering the high-excitation ^{12}CO and ^{13}CO lines in the PACS and SPIRE spectra.

3.2. Abundance profiles of SiO and SiS

The SiO and SiS emission lines are modelled with the thermodynamical structure as deduced in Sect. 3.1. Linelists and (available) collisional rates are described in Decin et al. (2010). However, the lack of collisional rates for high-J transitions of both molecules with He or H_2 led us calculate the level populations in LTE. This approach is justified since most of the detected high-J lines originate in the stellar photosphere and in the inner wind envelope, where the high gas density and temperature ensure thermal equilibrium for the level populations. Pulsation driven shocks in the inner envelope may alter abundances predicted from equilibrium chemistry. The estimated uncertainty on the derived abundances is a factor of 5, when taking the line flux uncertainty into account.

Table 1. Parameters for the best-fit model, where numbers in italics indicate input parameters that have been kept fixed at the given value.

$T_{\rm eff}$[K]	*2050*[a]	$\dot{M}[M_\odot/{\rm yr}]$	1×10^{-5}
$R_\star$ [10^{13} cm]	5	$R_{\rm dust}$ [$R_\star$]	*5.6*[d]
[CO/H_2] [10^{-3}]	*1*[b]	^{12}CO/^{13}CO	30
distance [pc]	*150*[c]	n(SiO)/n(H_2)	1×10^{-7}
v_∞ [km s^{-1}]	*14.5*	n(SiS)/n(H_2)	4×10^{-6}

References. [(a)] González-Alfonso et al. (2007), [(b)] Zuckerman & Dyck (1986), [(c)] Crosas & Menten (1997), [(d)] Ridgway & Keady (1988).

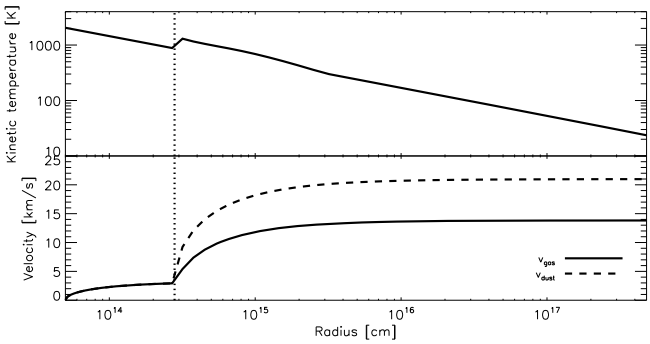

Fig. 2. Thermodynamical structure in the envelope of IRC +10216 as derived from the ^{12}CO rotational line transitions. The vertical dotted line represents the dust condensation radius.

SiO: Using an outer radius value of $560\,R_\star$ (Olofsson et al. 1982), the derived fractional abundance is [SiO/H_2] = 1×10^{-7}, when assuming a constant abundance profile. The high-J SiO lines in the PACS and SPIRE spectrum provide us with a diagnostic tool for deducing possible depletion from the gas from accretion onto dust grains. Unfortunately, the low signal-to-noise ratio of the (weak) high-excitation SiO lines prohibit us from putting strong constraints on the role of SiO in the dust formation around IRC +10216. When allowing for variations in the abundance profile (as described in Decin et al. 2010), we deduce that the SiO fractional abundance in the inner wind ($R \lesssim 8\,R_\star$) can range between $0.2-3 \times 10^{-7}$, with the fractional abundance being 1×10^{-7} beyond $8\,R_\star$ (see Fig. 3). Keady & Ridgway (1993) derived an inner wind SiO abundance of 8×10^{-7} from infrared ro-vibrational transitions. From low-excitation SiO lines, Schöier et al. (2006) obtained an SiO abundance in the region between ~3 and $8\,R_\star$, as high as $\sim 1.5 \times 10^{-6}$, superposed on a more spatially extended region of $480\,R_\star$ with a fractional abundance of 1.7×10^{-7}. The abundance in this compact inner-wind region is a factor 5 higher than our maximum deduced value of 3×10^{-7} in the inner wind. The theoretically calculated photospheric TE value of SiO in carbon-rich envelopes is $\sim 2.8 \times 10^{-8}$ (Willacy & Cherchneff 1998). In their study of the effect of

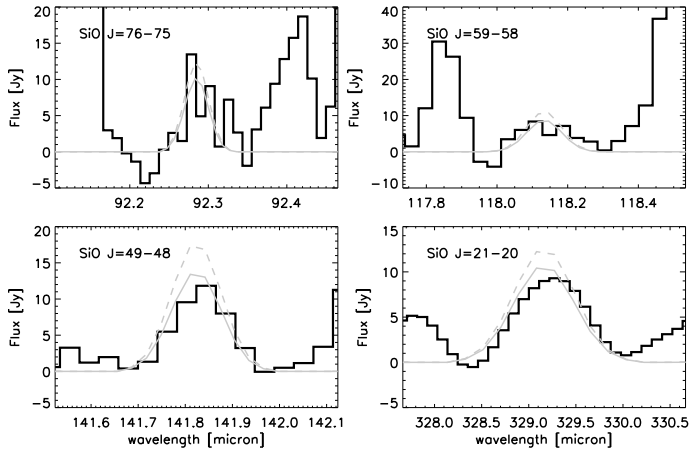

Fig. 3. Comparison between few PACS and SPIRE SiO $v = 0$ lines (black) and theoretical line predictions (grey). Full grey lines represent theoretical line profiles using a constant SiO fractional abundance of $[SiO/H_2] = 1 \times 10^{-7}$, and dashed grey lines represent model predictions simulating an inner wind abundance of $[SiO/H_2] = 3 \times 10^{-7}$ for $R < 8\,R_\star$ and 1×10^{-7} beyond that radius.

pulsationally induced non-chemical equilibrium in the inner wind of IRC +10216, Willacy & Cherchneff (1998) obtained a fractional abundance of 3.8×10^{-7}. Since TE-value agrees with our minimum deduced value in the inner wind of 2×10^{-8}, and the non-TE value with the maximum deduced value, the effect of pulsationally induced non-equilibrium chemistry is difficult to estimate.

SiS: The SiS fractional abundances derived from the PACS and SPIRE observations is $[SiS/H_2] = 4 \times 10^{-6}$. When taking the abundance uncertainty into account, this agrees with the results of Schöier et al. (2007), who find a value of 2×10^{-6} from low-excitation SiS lines. From observations of the 13.5 μm fundamental band of SiS, Boyle et al. (1994) obtained a gradient in the abundance of SiS, going from 4.3×10^{-6} at a distance of $12\,R_\star$ and rising to 4.3×10^{-5} close to the stellar surface. Bieging & Nguyen-Quang-Rieu (1989) obtained a much lower value of $[SiS/H_2] = 7.5 \times 10^{-6}$ for $R < 3 \times 10^{15}$ cm and 6.5×10^{-7} beyond that radius. The PACS and SPIRE observations can allow for a change of a factor of 2 in the first few stellar radii (i.e, minimum of 2×10^{-6}, maximum of 8×10^{-6} for $R \lesssim 12\,R_\star$). The SiS TE and non-TE inner wind values as computed by Willacy & Cherchneff (1998) are $[SiS/H_2] = 1.5 \times 10^{-5}$ and 3.4×10^{-5}, respectively. That our deduced SiS fractional abundance is clearly lower than the non-TE value of Willacy & Cherchneff (1998) might indicate toward uncertainties in the estimated rate values in Eqs. (11)−(13) in Willacy & Cherchneff (1998).

4. Conclusion

The PACS and SPIRE spectroscopic observations of IRC +10216 have been shown to be of excellent quality for studying the thermodynamical and chemical structure of the envelope, created by its copious mass loss. The temperature and mass-loss rate of the envelope are derived from the ^{12}CO lines. Both SiO and SiS are refractory species, and the PACS and SPIRE data can provide a strong diagnostic tool for determining their role in the dust formation process. Analysing the high-J SiO and SiS lines yields a constant fractional abundance of 1×10^{-7} and 4×10^{-6}, respectively. However, we detect only $v = 0$ and $v = 1$ transitions for both species, mainly because of the densely populated spectrum of IRC+10216, while it is known from ground-based observations that levels of SiS up to $v = 8$ have been detected (Agúndez et al. 2010, in prep.). Moreover, the low-J transitions of SiO and SiS, which are more sensitive to the external envelope, are not accesible to PACS and SPIRE. Since the high-J lines in the ground-state and the $v = 1$ lines of both molecules are very weak, we cannot put strong constraints on the fractional abundance in the inner envelope ($R \lesssim 10\,R_\star$). For SiO, 1/3 at most is estimated to take part in dust formation process, while we deduce a fraction of 1/2 for SiS. Only a merged set of millimeter, submillimeter, and far-infrared observations of SiO and SiS can provide a detailed analysis of the abundance of these species from the photosphere to the photodissociation zone (Agúndez et al. 2010, in prep.).

Acknowledgements. PACS was developed by a consortium of institutes led by MPE (Germany) and including UVIE (Austria); KUL, CSL, IMEC (Belgium); CEA, OAMP (France); MPIA (Germany); IFSI, OAP/AOT, OAA/CAISMI, LENS, SISSA (Italy); IAC (Spain). This development has been supported by the funding agencies BMVIT (Austria), ESA-PRODEX (Belgium), CEA/CNES (France), DLR (Germany), ASI (Italy), and CICT/MCT (Spain). SPIRE has been developed by a consortium of institutes led by Cardiff Univ. (UK) and including Univ. Lethbridge (Canada); NAOC (China); CEA, LAM (France); IFSI, Univ. Padua (Italy); IAC (Spain); Stockholm Observatory (Sweden); Imperial College London, RAL, UCL-MSSL, UKATC, Univ. Sussex (UK); Caltech, JPL, NHSC, Univ. Colorado (USA). This development has been supported by national funding agencies: CSA (Canada); NAOC (China); CEA, CNES, CNRS (France); ASI (Italy); MCINN (Spain); SNSB (Sweden); STFC (UK); and NASA (USA). L.D. acknowledges financial support from the Fund for Scientific Research – Flanders (FWO). M.G., D.L,. J.B., W.D.M., K.E., R.H., C.H., S.R., P.R., and B.V. acknowledge support from the Belgian Federal Science Policy Office via the PRODEX Programme of ESA. F.K. acknowledges funding by the Austrian Science Fund FWF under project number P18939-N16 and I163-N16

References

Barnes, T. G., Hinkle, K. H., Lambert, D. L., & Beer, R. 1977, ApJ, 213, 71
Bieging, J. H., & Nguyen-Quang-Rieu. 1989, ApJ, 343, L25
Boyle, R. J., Keady, J. J., Jennings, D. E., et al. 1994, ApJ, 420, 863
Cernicharo, J., Barlow, M. J., Gonzalez-Alfonso, E., et al. 1996, A&A, 315, L201
Cernicharo, J., Guélin, M., & Kahane, C. 2000, A&AS, 142, 181
Cernicharo, J., Decin, L., Barlow, M., et al. 2010, A&A, 518, L136
Crosas, M., & Menten, K. M. 1997, ApJ, 483, 913
De Beck, E., Decin, L., de Koter, A., et al. 2010, A&A, submitted
Decin, L., Hony, S., de Koter, A., et al. 2006, A&A, 456, 549
Decin, L., Hony, S., de Koter, A., et al. 2007, A&A, 475, 233
Decin, L., De Beck, E., Brunken, S., et al. 2010, A&A, 516, A69
Fonfría, J. P., Cernicharo, J., Richter, M. J., & Lacy, J. H. 2008, ApJ, 673, 445
González-Alfonso, E., Neufeld, D. A., & Melnick, G. J. 2007, ApJ, 669, 412
Griffin, M. J., Abergel, A., Abreu, A., et al. 2010, A&A, 518, L3
He, J. H., Dinh-V-Trung, K. S., Müller, H. S. P., et al. 2008, ApJS, 177, 275
Keady, J. J., & Ridgway, S. T. 1993, ApJ, 406, 199
Ladjal, D., Barlow, M., Groenewegen, M., et al. 2010, A&A, 518, L141
Mamon, G. A., Glassgold, A. E., & Huggins, P. J. 1988, ApJ, 328, 797
Naylor, D. A., & Tahic, M. K. 2007, J. of Optical Soc. of America A, 24, 3644
Olofsson, H., Johansson, L. E. B., Hjalmarson, A., & Nguyen-Quang-Rieu. 1982, A&A, 107, 128
Pilbratt, G. L., Riedinger, J. R., Passvogel, T., et al. 2010, A&A, 518, L1
Poglitsch, A., Waelkens, C., Geis, N., et al. 2010, A&A, 518, L2
Ridgway, S., & Keady, J. J. 1988, ApJ, 326, 843
Royer, P., Decin, L., Wesson, R., et al. 2010, A&A, 518, L145
Schöier, F. L., & Olofsson, H. 2000, A&A, 359, 586
Schöier, F. L., Fong, D., Olofsson, H., et al. 2006, ApJ, 649, 965
Schöier, F. L., Bast, J., Olofsson, H., & Lindqvist, M. 2007, A&A, 473, 871
Skinner, C. J., Meixner, M., & Bobrowsky, M. 1998, MNRAS, 300, L29
Swinyard, B. M., Ade, P., Baluteau, J.-P., et al. 2010, A&A, 518, L4
Willacy, K., & Cherchneff, I. 1998, A&A, 330, 676
Zuckerman, B., & Dyck, H. M. 1986, ApJ, 304, 394

Pages 5 to 11 are available in the electronic edition of the journal at http://www.aanda.org

[1] Instituut voor Sterrenkunde, Katholieke Universiteit Leuven, Celestijnenlaan 200D, 3001 Leuven, Belgium
e-mail: Leen.Decin@ster.kuleuven.be
[2] Sterrenkundig Instituut Anton Pannekoek, University of Amsterdam, Science Park 904, 1098 Amsterdam, The Netherlands
[3] Laboratory of Molecular Astrophysics, Department of Astrophysics, CAB, INTA-CSIC, Ctra de Ajalvir, km 4, 28850 Torrejon de Ardoz, Madrid, Spain
[4] Dept of Physics & Astronomy, University College London, Gower St, London WC1E 6BT, UK
[5] Space Science and Technology Department, Rutherford Appleton Laboratory, Oxfordshire, OX11 0QX, UK
[6] Department of Physics, University of Lethbridge, Lethbridge, Alberta, T1J 1B1, Canada
[7] Departamento de Astrofísica Molecular e Infrarroja, Instituto de Estructura de la Materia, CSIC, Serrano 121, 28006 Madrid, Spain
[8] Radio Astronomy Laboratory, University of California at Berkeley, CA 94720, USA
[9] LUTH, Observatoire de Paris-Meudon, 5 Place Jules Janssen, 92190 Meudon, France
[10] Max-Planck-Institut für extraterrestrische Physik, 85748 Giessenbachstrasse, Germany
[11] School of Physics and Astronomy, Cardiff University, Queens Buildings, The Parade, Cardiff, CF24 3AA, UK
[12] Royal Observatory of Belgium, Ringlaan 3, 1180 Brussels, Belgium
[13] Blue Sky Spectroscopy, 9/740 4 Ave S, Lethbridge, Alberta T1J 0N9, Canada
[14] UK Astronomy Technology Centre, Royal Observatory Edinburgh, Blackford Hill, Edinburgh EH9 3HJ, UK
[15] Dept of Astronomy, Stockholm University, AlbaNova University Center, Roslagstullsbacken 21, 10691 Stockholm, Sweden
[16] University of Vienna, Department of Astronomy, Türkenschanzstraße 17, 1180 Vienna, Austria
[17] Mullard Space Science Laboratory, University College London, Holmbury St. Mary, Dorking, Surrey RH5 6NT, UK

Appendix A: Identified lines of $^{12}C^{16}O$, $^{13}C^{16}O$, $^{28}Si^{16}O$, and $^{28}Si^{32}S$

Table A.1. Identified lines of $^{12}C^{16}O$, $^{13}C^{16}O$, $^{28}Si^{16}O$, and $^{28}Si^{32}S$ in the PACS and SPIRE spectrum of IRC 10216.

Molecule	Transition	Frequency [GHz]	Wavelength [μm]	Integrated Flux [erg/cm^2/s]	Blend
$^{12}C^{16}O$	$v = 0–0$, $J = 4–3$	461.042	650.250	1.35e-12	no
$^{12}C^{16}O$	$v = 0–0$, $J = 5–4$	576.267	520.232	2.20e-12	no
$^{12}C^{16}O$	$v = 0–0$, $J = 6–5$	691.474	433.555	3.08e-12	no
$^{12}C^{16}O$	$v = 0–0$, $J = 7–6$	806.652	371.650	4.17e-12	no
$^{12}C^{16}O$	$v = 0–0$, $J = 8–7$	921.799	325.225	4.98e-12	no
$^{12}C^{16}O$	$v = 0–0$, $J = 9–8$	1036.913	289.120	6.01e-12	no
$^{12}C^{16}O$	$v = 0–0$, $J = 10–9$	1151.986	260.240	6.67e-12	no
$^{12}C^{16}O$	$v = 0–0$, $J = 11–10$	1267.016	236.613	7.22e-12	no
$^{12}C^{16}O$	$v = 0–0$, $J = 12–11$	1381.995	216.927	1.98e-12	no
$^{12}C^{16}O$	$v = 0–0$, $J = 13–12$	1496.924	200.272	2.99e-12	no
$^{12}C^{16}O$	$v = 0–0$, $J = 14–13$	1611.792	185.999	7.36e-12	no
$^{12}C^{16}O$	$v = 0–0$, $J = 15–14$	1726.604	173.631	7.31e-12	no
$^{12}C^{16}O$	$v = 0–0$, $J = 16–15$	1841.347	162.812	7.32e-12	no
$^{12}C^{16}O$	$v = 0–0$, $J = 17–16$	1956.017	153.267	6.95e-12	no
$^{12}C^{16}O$	$v = 0–0$, $J = 18–17$	2070.616	144.784	6.68e-12	no
$^{12}C^{16}O$	$v = 0–0$, $J = 19–18$	2185.134	137.196	6.47e-12	no
$^{12}C^{16}O$	$v = 0–0$, $J = 20–19$	2299.570	130.369	6.15e-12	no
$^{12}C^{16}O$	$v = 0–0$, $J = 21–20$	2413.917	124.193	5.88e-12	no
$^{12}C^{16}O$	$v = 0–0$, $J = 22–21$	2528.171	118.581	5.53e-12	no
$^{12}C^{16}O$	$v = 0–0$, $J = 23–22$	2642.332	113.458	5.08e-12	no
$^{12}C^{16}O$	$v = 0–0$, $J = 24–23$	2756.388	108.763	4.83e-12	no
$^{12}C^{16}O$	$v = 0–0$, $J = 25–24$	2870.339	104.445	4.51e-12	no
$^{12}C^{16}O$	$v = 0–0$, $J = 27–26$	3097.909	96.773	4.06e-12	no
$^{12}C^{16}O$	$v = 0–0$, $J = 28–27$	3211.518	93.349	3.85e-12	no
$^{12}C^{16}O$	$v = 0–0$, $J = 29–28$	3325.005	90.163	3.55e-12	yes
$^{12}C^{16}O$	$v = 0–0$, $J = 30–29$	3438.365	87.190	3.38e-12	yes
$^{12}C^{16}O$	$v = 0–0$, $J = 31–30$	3551.594	84.411	3.09e-12	no
$^{12}C^{16}O$	$v = 0–0$, $J = 32–31$	3664.685	81.806	2.95e-12	no
$^{12}C^{16}O$	$v = 0–0$, $J = 33–32$	3777.637	79.360	2.68e-12	no
$^{12}C^{16}O$	$v = 0–0$, $J = 34–33$	3890.443	77.059	2.59e-12	no
$^{12}C^{16}O$	$v = 0–0$, $J = 35–34$	4003.102	74.890	2.31e-12	no
$^{12}C^{16}O$	$v = 0–0$, $J = 36–35$	4115.605	72.843	2.18e-12	no
$^{12}C^{16}O$	$v = 0–0$, $J = 37–36$	4227.953	70.907	2.05e-12	yes
$^{12}C^{16}O$	$v = 0–0$, $J = 38–37$	4340.138	69.074	1.89e-12	no
$^{12}C^{16}O$	$v = 0–0$, $J = 39–38$	4452.159	67.336	1.74e-12	no
$^{12}C^{16}O$	$v = 0–0$, $J = 40–39$	4564.005	65.686	1.60e-12	no
$^{12}C^{16}O$	$v = 0–0$, $J = 41–40$	4675.681	64.117	1.50e-12	no
$^{12}C^{16}O$	$v = 0–0$, $J = 42–41$	4787.174	62.624	1.34e-12	no
$^{12}C^{16}O$	$v = 0–0$, $J = 43–42$	4898.484	61.201	1.31e-12	no
$^{12}C^{16}O$	$v = 0–0$, $J = 44–43$	5009.608	59.843	1.18e-12	yes
$^{12}C^{16}O$	$v = 0–0$, $J = 45–44$	5120.540	58.547	1.12e-12	no
$^{12}C^{16}O$	$v = 1–1$, $J = 28–27$	3182.136	94.211	1.42e-13	yes
$^{12}C^{16}O$	$v = 1–1$, $J = 29–28$	3294.573	90.996	1.41e-13	yes
$^{12}C^{16}O$	$v = 1–1$, $J = 30–29$	3406.884	87.996	1.51e-13	no
$^{12}C^{16}O$	$v = 1–1$, $J = 31–30$	3519.060	85.191	1.48e-13	no
$^{12}C^{16}O$	$v = 1–1$, $J = 32–31$	3631.105	82.562	1.51e-13	no
$^{13}C^{16}O$	$v = 0–0$, $J = 5–4$	550.926	544.161	1.17e-13	yes
$^{13}C^{16}O$	$v = 0–0$, $J = 6–5$	661.066	453.498	1.75e-13	no
$^{13}C^{16}O$	$v = 0–0$, $J = 7–6$	771.183	388.743	2.39e-13	yes
$^{13}C^{16}O$	$v = 0–0$, $J = 8–7$	881.273	340.181	3.19e-13	yes
$^{13}C^{16}O$	$v = 0–0$, $J = 9–8$	991.330	302.414	4.05e-13	no
$^{13}C^{16}O$	$v = 0–0$, $J = 10–9$	1101.351	272.204	4.85e-13	no
$^{13}C^{16}O$	$v = 0–0$, $J = 11–10$	1211.330	247.490	5.39e-13	no

Table A.1. continued.

Molecule	Transition	Frequency [GHz]	Wavelength [μm]	Integrated Flux [erg/cm^2/s]	Blend
$^{13}C^{16}O$	$v = 0–0$, $J = 12–11$	1321.267	226.898	6.11e-13	yes
$^{13}C^{16}O$	$v = 0–0$, $J = 13–12$	1431.152	209.476	6.27e-13	no
$^{13}C^{16}O$	$v = 0–0$, $J = 14–13$	1540.987	194.546	2.91e-13	no
$^{13}C^{16}O$	$v = 0–0$, $J = 15–14$	1650.768	181.608	6.94e-13	no
$^{13}C^{16}O$	$v = 0–0$, $J = 16–15$	1760.487	170.290	6.99e-13	no
$^{13}C^{16}O$	$v = 0–0$, $J = 17–16$	1870.142	160.305	7.05e-13	no
$^{13}C^{16}O$	$v = 0–0$, $J = 18–17$	1979.728	151.431	7.03e-13	no
$^{13}C^{16}O$	$v = 0–0$, $J = 19–18$	2089.239	143.494	6.87e-13	no
$^{13}C^{16}O$	$v = 0–0$, $J = 20–19$	2198.678	136.351	6.68e-13	no
$^{13}C^{16}O$	$v = 0–0$, $J = 21–20$	2308.034	129.891	6.32e-13	yes
$^{13}C^{16}O$	$v = 0–0$, $J = 22–21$	2417.308	124.019	6.36e-13	yes
$^{13}C^{16}O$	$v = 0–0$, $J = 23–22$	2526.492	118.660	5.93e-13	yes
$^{13}C^{16}O$	$v = 0–0$, $J = 24–23$	2635.584	113.748	5.73e-13	no
$^{13}C^{16}O$	$v = 0–0$, $J = 25–24$	2744.579	109.231	5.63e-13	no
$^{13}C^{16}O$	$v = 0–0$, $J = 26–25$	2853.476	105.062	5.39e-13	no
$^{13}C^{16}O$	$v = 0–0$, $J = 28–27$	3070.949	97.622	4.90e-13	no
$^{13}C^{16}O$	$v = 0–0$, $J = 29–28$	3179.518	94.289	4.75e-13	no
$^{13}C^{16}O$	$v = 0–0$, $J = 30–29$	3287.974	91.178	4.58e-13	no
$^{13}C^{16}O$	$v = 0–0$, $J = 31–30$	3396.307	88.270	4.39e-13	no
$^{13}C^{16}O$	$v = 0–0$, $J = 32–31$	3504.517	85.545	4.22e-13	no
$^{13}C^{16}O$	$v = 0–0$, $J = 33–32$	3612.599	82.985	4.11e-13	yes
$^{13}C^{16}O$	$v = 0–0$, $J = 34–33$	3720.548	80.578	3.97e-13	no
$^{13}C^{16}O$	$v = 0–0$, $J = 35–34$	3828.359	78.308	3.83e-13	no
$^{13}C^{16}O$	$v = 0–0$, $J = 36–35$	3936.033	76.166	3.72e-13	no
$^{13}C^{16}O$	$v = 0–0$, $J = 37–36$	4043.562	74.141	3.63e-13	yes
$^{13}C^{16}O$	$v = 0–0$, $J = 38–37$	4150.945	72.223	3.54e-13	yes
$^{13}C^{16}O$	$v = 0–0$, $J = 39–38$	4258.172	70.404	3.52e-13	no
$^{13}C^{16}O$	$v = 0–0$, $J = 40–39$	4365.246	68.677	3.35e-13	no
$^{13}C^{16}O$	$v = 0–0$, $J = 41–40$	4472.161	67.035	3.33e-13	no
$^{13}C^{16}O$	$v = 0–0$, $J = 42–41$	4578.908	65.472	3.11e-13	no
$^{13}C^{16}O$	$v = 0–0$, $J = 43–42$	4685.490	63.983	3.16e-13	no
$^{13}C^{16}O$	$v = 0–0$, $J = 44–43$	4791.901	62.562	3.03e-13	no
$^{28}Si^{16}O$	$v = 0–0$, $J = 11–10$	477.569	627.746	7.26e-14	no
$^{28}Si^{16}O$	$v = 0–0$, $J = 12–11$	520.740	575.705	9.52e-14	no
$^{28}Si^{16}O$	$v = 0–0$, $J = 13–12$	564.209	531.350	1.19e-13	no
$^{28}Si^{16}O$	$v = 0–0$, $J = 14–13$	607.679	493.340	1.41e-13	no
$^{28}Si^{16}O$	$v = 0–0$, $J = 15–14$	650.850	460.617	1.62e-13	no
$^{28}Si^{16}O$	$v = 0–0$, $J = 16–15$	694.319	431.779	1.81e-13	no
$^{28}Si^{16}O$	$v = 0–0$, $J = 17–16$	737.490	406.504	1.94e-13	no
$^{28}Si^{16}O$	$v = 0–0$, $J = 18–17$	780.959	383.877	2.11e-13	no
$^{28}Si^{16}O$	$v = 0–0$, $J = 19–18$	824.130	363.769	2.16e-13	no
$^{28}Si^{16}O$	$v = 0–0$, $J = 20–19$	867.600	345.542	2.29e-13	no
$^{28}Si^{16}O$	$v = 0–0$, $J = 21–20$	910.770	329.164	2.33e-13	no
$^{28}Si^{16}O$	$v = 0–0$, $J = 22–21$	953.940	314.268	2.46e-13	no
$^{28}Si^{16}O$	$v = 0–0$, $J = 23–22$	997.410	300.571	2.49e-13	no
$^{28}Si^{16}O$	$v = 0–0$, $J = 24–23$	1040.580	288.101	2.57e-13	no
$^{28}Si^{16}O$	$v = 0–0$, $J = 25–24$	1083.750	276.625	2.57e-13	no
$^{28}Si^{16}O$	$v = 0–0$, $J = 26–25$	1126.920	266.028	2.55e-13	no
$^{28}Si^{16}O$	$v = 0–0$, $J = 27–26$	1170.090	256.213	2.64e-13	no
$^{28}Si^{16}O$	$v = 0–0$, $J = 28–27$	1213.260	247.097	2.66e-13	yes
$^{28}Si^{16}O$	$v = 0–0$, $J = 29–28$	1256.430	238.606	2.60e-13	no
$^{28}Si^{16}O$	$v = 0–0$, $J = 30–29$	1299.601	230.680	2.66e-13	yes
$^{28}Si^{16}O$	$v = 0–0$, $J = 31–30$	1342.471	223.314	2.62e-13	no
$^{28}Si^{16}O$	$v = 0–0$, $J = 32–31$	1385.641	216.357	7.17e-14	yes
$^{28}Si^{16}O$	$v = 0–0$, $J = 33–32$	1428.811	209.820	2.73e-13	no
$^{28}Si^{16}O$	$v = 0–0$, $J = 34–33$	1471.681	203.707	9.86e-14	no

Table A.1. continued.

Molecule	Transition	Frequency [GHz]	Wavelength [μm]	Integrated Flux [erg/cm^2/s]	Blend
$^{28}Si^{16}O$	$v = 0–0$, $J = 35–34$	1514.852	197.902	2.75e-13	yes
$^{28}Si^{16}O$	$v = 0–0$, $J = 36–35$	1557.722	192.456	1.22e-13	no
$^{28}Si^{16}O$	$v = 0–0$, $J = 37–36$	1600.592	187.301	2.75e-13	yes
$^{28}Si^{16}O$	$v = 0–0$, $J = 38–37$	1643.762	182.382	2.70e-13	no
$^{28}Si^{16}O$	$v = 0–0$, $J = 39–38$	1686.633	177.746	2.73e-13	yes
$^{28}Si^{16}O$	$v = 0–0$, $J = 40–39$	1729.503	173.340	2.77e-13	no
$^{28}Si^{16}O$	$v = 0–0$, $J = 41–40$	1772.373	169.147	2.75e-13	no
$^{28}Si^{16}O$	$v = 0–0$, $J = 42–41$	1814.944	165.180	2.79e-13	no
$^{28}Si^{16}O$	$v = 0–0$, $J = 43–42$	1857.814	161.368	2.78e-13	yes
$^{28}Si^{16}O$	$v = 0–0$, $J = 44–43$	1900.684	157.729	2.77e-13	yes
$^{28}Si^{16}O$	$v = 0–0$, $J = 45–44$	1943.255	154.273	2.69e-13	no
$^{28}Si^{16}O$	$v = 0–0$, $J = 46–45$	1986.125	150.943	2.68e-13	no
$^{28}Si^{16}O$	$v = 0–0$, $J = 47–46$	2028.696	147.776	2.70e-13	no
$^{28}Si^{16}O$	$v = 0–0$, $J = 48–47$	2071.266	144.739	2.73e-13	yes
$^{28}Si^{16}O$	$v = 0–0$, $J = 49–48$	2113.837	141.824	2.64e-13	no
$^{28}Si^{16}O$	$v = 0–0$, $J = 50–49$	2156.408	139.024	2.69e-13	no
$^{28}Si^{16}O$	$v = 0–0$, $J = 51–50$	2198.978	136.333	2.60e-13	yes
$^{28}Si^{16}O$	$v = 0–0$, $J = 52–51$	2241.549	133.743	2.62e-13	no
$^{28}Si^{16}O$	$v = 0–0$, $J = 53–52$	2283.819	131.268	2.59e-13	yes
$^{28}Si^{16}O$	$v = 0–0$, $J = 54–53$	2326.390	128.866	2.48e-13	yes
$^{28}Si^{16}O$	$v = 0–0$, $J = 55–54$	2368.661	126.566	2.51e-13	yes
$^{28}Si^{16}O$	$v = 0–0$, $J = 56–55$	2410.931	124.347	2.48e-13	yes
$^{28}Si^{16}O$	$v = 0–0$, $J = 57–56$	2453.202	122.205	2.43e-13	no
$^{28}Si^{16}O$	$v = 0–0$, $J = 58–57$	2495.473	120.135	2.37e-13	yes
$^{28}Si^{16}O$	$v = 0–0$, $J = 59–58$	2537.744	118.133	2.27e-13	no
$^{28}Si^{16}O$	$v = 0–0$, $J = 60–59$	2580.014	116.198	2.27e-13	yes
$^{28}Si^{16}O$	$v = 0–0$, $J = 61–60$	2621.985	114.338	2.23e-13	yes
$^{28}Si^{16}O$	$v = 0–0$, $J = 62–61$	2664.256	112.524	2.17e-13	yes
$^{28}Si^{16}O$	$v = 0–0$, $J = 63–62$	2706.227	110.779	2.10e-13	no
$^{28}Si^{16}O$	$v = 0–0$, $J = 64–63$	2748.198	109.087	2.05e-13	yes
$^{28}Si^{16}O$	$v = 0–0$, $J = 65–64$	2790.169	107.446	2.01e-13	no
$^{28}Si^{16}O$	$v = 0–0$, $J = 66–65$	2832.140	105.854	1.94e-13	yes
$^{28}Si^{16}O$	$v = 0–0$, $J = 67–66$	2874.111	104.308	1.84e-13	yes
$^{28}Si^{16}O$	$v = 0–0$, $J = 68–67$	2915.782	102.817	1.80e-13	yes
$^{28}Si^{16}O$	$v = 0–0$, $J = 72–71$	3082.467	97.257	1.56e-13	no
$^{28}Si^{16}O$	$v = 0–0$, $J = 73–72$	3124.138	95.960	1.52e-13	yes
$^{28}Si^{16}O$	$v = 0–0$, $J = 74–73$	3165.809	94.697	1.46e-13	yes
$^{28}Si^{16}O$	$v = 0–0$, $J = 75–74$	3207.180	93.475	1.37e-13	yes
$^{28}Si^{16}O$	$v = 0–0$, $J = 76–75$	3248.552	92.285	1.34e-13	no
$^{28}Si^{16}O$	$v = 0–0$, $J = 77–76$	3289.923	91.124	1.28e-13	yes
$^{28}Si^{16}O$	$v = 0–0$, $J = 78–77$	3331.294	89.993	1.19e-13	yes
$^{28}Si^{16}O$	$v = 0–0$, $J = 79–78$	3372.666	88.889	1.17e-13	no
$^{28}Si^{16}O$	$v = 0–0$, $J = 80–79$	3413.737	87.819	1.13e-13	yes
$^{28}Si^{16}O$	$v = 0–0$, $J = 81–80$	3454.809	86.775	1.08e-13	yes
$^{28}Si^{16}O$	$v = 0–0$, $J = 82–81$	3496.180	85.749	1.03e-13	yes
$^{28}Si^{16}O$	$v = 0–0$, $J = 83–82$	3536.952	84.760	9.76e-14	yes
$^{28}Si^{16}O$	$v = 0–0$, $J = 84–83$	3578.024	83.787	9.20e-14	yes
$^{28}Si^{16}O$	$v = 0–0$, $J = 85–84$	3619.095	82.836	8.84e-14	yes
$^{28}Si^{16}O$	$v = 0–0$, $J = 86–85$	3659.867	81.913	8.23e-14	yes
$^{28}Si^{16}O$	$v = 0–0$, $J = 87–86$	3700.639	81.011	8.11e-14	yes
$^{28}Si^{16}O$	$v = 0–0$, $J = 88–87$	3741.410	80.128	7.74e-14	yes
$^{28}Si^{16}O$	$v = 0–0$, $J = 89–88$	3782.182	79.264	7.36e-14	yes
$^{28}Si^{16}O$	$v = 0–0$, $J = 90–89$	3822.654	78.425	7.13e-14	yes
$^{28}Si^{16}O$	$v = 1–1$, $J = 39–38$	1674.641	179.019	4.06e-14	yes
$^{28}Si^{16}O$	$v = 1–1$, $J = 40–39$	1717.211	174.581	4.28e-14	yes
$^{28}Si^{16}O$	$v = 1–1$, $J = 41–40$	1759.782	170.358	4.40e-14	yes

Table A.1. continued.

Molecule	Transition	Frequency [GHz]	Wavelength [μm]	Integrated Flux [erg/cm^2/s]	Blend
^{28}Si^{16}O	v = 1−1, J = 42−41	1802.353	166.334	4.74e-14	no
^{28}Si^{16}O	v = 1−1, J = 43−42	1844.923	162.496	4.88e-14	yes
^{28}Si^{16}O	v = 1−1, J = 44−43	1887.194	158.856	5.15e-14	yes
^{28}Si^{16}O	v = 1−1, J = 45−44	1929.764	155.352	5.28e-14	no
^{28}Si^{16}O	v = 1−1, J = 46−45	1972.035	152.022	5.48e-14	yes
^{28}Si^{16}O	v = 1−1, J = 47−46	2014.606	148.809	5.53e-14	yes
^{28}Si^{16}O	v = 1−1, J = 48−47	2056.876	145.751	5.64e-14	yes
^{28}Si^{16}O	v = 1−1, J = 49−48	2099.147	142.816	5.82e-14	no
^{28}Si^{32}S	v = 0−0, J = 26−25	471.608	635.682	1.29e-13	yes
^{28}Si^{32}S	v = 0−0, J = 27−26	489.713	612.180	1.45e-13	yes
^{28}Si^{32}S	v = 0−0, J = 28−27	507.813	590.360	1.47e-13	no
^{28}Si^{32}S	v = 0−0, J = 29−28	525.910	570.045	1.61e-13	no
^{28}Si^{32}S	v = 0−0, J = 30−29	544.003	551.087	1.61e-13	no
^{28}Si^{32}S	v = 0−0, J = 31−30	562.091	533.352	1.76e-13	no
^{28}Si^{32}S	v = 0−0, J = 32−31	580.175	516.728	1.74e-13	no
^{28}Si^{32}S	v = 0−0, J = 33−32	598.254	501.112	1.85e-13	no
^{28}Si^{32}S	v = 0−0, J = 34−33	616.328	486.417	1.84e-13	no
^{28}Si^{32}S	v = 0−0, J = 35−34	634.398	472.562	1.91e-13	no
^{28}Si^{32}S	v = 0−0, J = 36−35	652.463	459.478	1.93e-13	no
^{28}Si^{32}S	v = 0−0, J = 37−36	670.522	447.103	1.93e-13	no
^{28}Si^{32}S	v = 0−0, J = 38−37	688.576	435.380	1.98e-13	no
^{28}Si^{32}S	v = 0−0, J = 39−38	706.625	424.260	1.93e-13	yes
^{28}Si^{32}S	v = 0−0, J = 40−39	724.668	413.696	2.00e-13	no
^{28}Si^{32}S	v = 0−0, J = 41−40	742.705	403.649	2.00e-13	no
^{28}Si^{32}S	v = 0−0, J = 42−41	760.737	394.082	1.97e-13	no
^{28}Si^{32}S	v = 0−0, J = 43−42	778.762	384.960	2.03e-13	no
^{28}Si^{32}S	v = 0−0, J = 44−43	796.782	376.254	2.00e-13	yes
^{28}Si^{32}S	v = 0−0, J = 45−44	814.795	367.936	1.99e-13	no
^{28}Si^{32}S	v = 0−0, J = 46−45	832.801	359.981	2.04e-13	yes
^{28}Si^{32}S	v = 0−0, J = 47−46	850.801	352.365	2.02e-13	no
^{28}Si^{32}S	v = 0−0, J = 48−47	868.795	345.067	1.98e-13	no
^{28}Si^{32}S	v = 0−0, J = 49−48	886.781	338.068	2.04e-13	yes
^{28}Si^{32}S	v = 0−0, J = 50−49	904.760	331.350	2.05e-13	no
^{28}Si^{32}S	v = 0−0, J = 51−50	922.733	324.896	2.00e-13	yes
^{28}Si^{32}S	v = 0−0, J = 52−51	940.697	318.692	2.01e-13	no
^{28}Si^{32}S	v = 0−0, J = 53−52	958.655	312.722	2.06e-13	no
^{28}Si^{32}S	v = 0−0, J = 54−53	976.605	306.974	2.07e-13	yes
^{28}Si^{32}S	v = 0−0, J = 55−54	994.547	301.436	2.05e-13	no
^{28}Si^{32}S	v = 0−0, J = 56−55	1012.481	296.097	2.01e-13	no
^{28}Si^{32}S	v = 0−0, J = 57−56	1030.407	290.946	2.03e-13	no
^{28}Si^{32}S	v = 0−0, J = 58−57	1048.325	285.973	2.07e-13	no
^{28}Si^{32}S	v = 0−0, J = 59−58	1066.235	281.169	2.09e-13	yes
^{28}Si^{32}S	v = 0−0, J = 60−59	1084.136	276.527	2.09e-13	no
^{28}Si^{32}S	v = 0−0, J = 61−60	1102.029	272.037	2.09e-13	yes
^{28}Si^{32}S	v = 0−0, J = 62−61	1119.913	267.693	2.08e-13	yes
^{28}Si^{32}S	v = 0−0, J = 63−62	1137.788	263.487	2.07e-13	no
^{28}Si^{32}S	v = 0−0, J = 64−63	1155.654	259.414	2.06e-13	yes
^{28}Si^{32}S	v = 0−0, J = 65−64	1173.511	255.466	2.05e-13	yes
^{28}Si^{32}S	v = 0−0, J = 66−65	1191.358	251.639	2.04e-13	no
^{28}Si^{32}S	v = 0−0, J = 67−66	1209.196	247.927	2.04e-13	yes
^{28}Si^{32}S	v = 0−0, J = 68−67	1227.025	244.325	2.04e-13	no
^{28}Si^{32}S	v = 0−0, J = 69−68	1244.843	240.827	2.04e-13	yes
^{28}Si^{32}S	v = 0−0, J = 70−69	1262.652	237.431	2.05e-13	no
^{28}Si^{32}S	v = 0−0, J = 71−70	1280.451	234.130	2.05e-13	no
^{28}Si^{32}S	v = 0−0, J = 72−71	1298.240	230.922	2.06e-13	yes
^{28}Si^{32}S	v = 0−0, J = 73−72	1316.018	227.803	2.05e-13	no

Table A.1. continued.

Molecule	Transition	Frequency [GHz]	Wavelength [μm]	Integrated Flux [erg/cm^2/s]	Blend
$^{28}Si^{32}S$	$v = 0–0$, $J = 74–73$	1333.786	224.768	2.04e-13	yes
$^{28}Si^{32}S$	$v = 0–0$, $J = 75–74$	1351.543	221.815	2.00e-13	no
$^{28}Si^{32}S$	$v = 0–0$, $J = 76–75$	1369.290	218.940	4.81e-14	yes
$^{28}Si^{32}S$	$v = 0–0$, $J = 77–76$	1387.025	216.141	1.96e-13	yes
$^{28}Si^{32}S$	$v = 0–0$, $J = 78–77$	1404.750	213.413	5.78e-14	no
$^{28}Si^{32}S$	$v = 0–0$, $J = 79–78$	1422.463	210.756	1.97e-13	yes
$^{28}Si^{32}S$	$v = 0–0$, $J = 80–79$	1440.165	208.165	6.35e-14	no
$^{28}Si^{32}S$	$v = 0–0$, $J = 81–80$	1457.856	205.639	6.63e-14	no
$^{28}Si^{32}S$	$v = 0–0$, $J = 82–81$	1475.535	203.175	7.07e-14	no
$^{28}Si^{32}S$	$v = 0–0$, $J = 83–82$	1493.202	200.772	7.24e-14	yes
$^{28}Si^{32}S$	$v = 0–0$, $J = 84–83$	1510.858	198.425	1.83e-13	yes
$^{28}Si^{32}S$	$v = 0–0$, $J = 85–84$	1528.501	196.135	7.80e-14	no
$^{28}Si^{32}S$	$v = 0–0$, $J = 86–85$	1546.132	193.898	1.79e-13	no
$^{28}Si^{32}S$	$v = 0–0$, $J = 87–86$	1563.751	191.714	8.13e-14	no
$^{28}Si^{32}S$	$v = 0–0$, $J = 88–87$	1581.357	189.579	1.78e-13	yes
$^{28}Si^{32}S$	$v = 0–0$, $J = 89–88$	1598.951	187.493	1.71e-13	yes
$^{28}Si^{32}S$	$v = 0–0$, $J = 90–89$	1616.532	185.454	1.72e-13	no
$^{28}Si^{32}S$	$v = 0–0$, $J = 91–90$	1634.100	183.460	1.72e-13	no
$^{28}Si^{32}S$	$v = 0–0$, $J = 92–91$	1651.655	181.510	1.66e-13	yes
$^{28}Si^{32}S$	$v = 0–0$, $J = 93–92$	1669.197	179.603	1.65e-13	yes
$^{28}Si^{32}S$	$v = 0–0$, $J = 94–93$	1686.725	177.736	1.60e-13	yes
$^{28}Si^{32}S$	$v = 0–0$, $J = 95–94$	1704.240	175.910	1.60e-13	no
$^{28}Si^{32}S$	$v = 0–0$, $J = 96–95$	1721.742	174.122	1.55e-13	no
$^{28}Si^{32}S$	$v = 0–0$, $J = 97–96$	1739.229	172.371	1.55e-13	no
$^{28}Si^{32}S$	$v = 0–0$, $J = 98–97$	1756.703	170.656	1.53e-13	yes
$^{28}Si^{32}S$	$v = 0–0$, $J = 99–98$	1774.163	168.977	1.48e-13	yes
$^{28}Si^{32}S$	$v = 0–0$, $J = 100–99$	1791.608	167.331	1.44e-13	yes
$^{28}Si^{32}S$	$v = 0–0$, $J = 101–100$	1809.039	165.719	1.42e-13	yes
$^{28}Si^{32}S$	$v = 0–0$, $J = 102–101$	1826.456	164.139	1.41e-13	no
$^{28}Si^{32}S$	$v = 0–0$, $J = 103–102$	1843.858	162.590	1.36e-13	yes
$^{28}Si^{32}S$	$v = 0–0$, $J = 104–103$	1861.245	161.071	1.31e-13	no
$^{28}Si^{32}S$	$v = 0–0$, $J = 105–104$	1878.618	159.581	1.32e-13	no
$^{28}Si^{32}S$	$v = 0–0$, $J = 106–105$	1895.975	158.120	1.27e-13	yes
$^{28}Si^{32}S$	$v = 0–0$, $J = 107–106$	1913.318	156.687	1.26e-13	no
$^{28}Si^{32}S$	$v = 0–0$, $J = 108–107$	1930.644	155.281	1.19e-13	yes
$^{28}Si^{32}S$	$v = 0–0$, $J = 109–108$	1947.956	153.901	1.17e-13	yes
$^{28}Si^{32}S$	$v = 0–0$, $J = 110–109$	1965.251	152.547	1.13e-13	no
$^{28}Si^{32}S$	$v = 0–0$, $J = 111–110$	1982.531	151.217	1.15e-13	yes
$^{28}Si^{32}S$	$v = 0–0$, $J = 112–111$	1999.795	149.912	1.08e-13	yes
$^{28}Si^{32}S$	$v = 0–0$, $J = 113–112$	2017.043	148.630	1.06e-13	no
$^{28}Si^{32}S$	$v = 0–0$, $J = 114–113$	2034.275	147.371	1.03e-13	yes
$^{28}Si^{32}S$	$v = 0–0$, $J = 115–114$	2051.491	146.134	1.03e-13	no
$^{28}Si^{32}S$	$v = 0–0$, $J = 116–115$	2068.690	144.919	1.00e-13	yes
$^{28}Si^{32}S$	$v = 0–0$, $J = 117–116$	2085.872	143.725	9.45e-14	no
$^{28}Si^{32}S$	$v = 0–0$, $J = 118–117$	2103.037	142.552	9.44e-14	no
$^{28}Si^{32}S$	$v = 0–0$, $J = 119–118$	2120.186	141.399	9.06e-14	yes
$^{28}Si^{32}S$	$v = 0–0$, $J = 120–119$	2137.318	140.266	8.85e-14	yes
$^{28}Si^{32}S$	$v = 0–0$, $J = 121–120$	2154.432	139.151	8.56e-14	yes
$^{28}Si^{32}S$	$v = 0–0$, $J = 122–121$	2171.529	138.056	8.17e-14	no
$^{28}Si^{32}S$	$v = 0–0$, $J = 123–122$	2188.609	136.979	7.89e-14	yes
$^{28}Si^{32}S$	$v = 0–0$, $J = 124–123$	2205.671	135.919	7.78e-14	yes
$^{28}Si^{32}S$	$v = 1–1$, $J = 50–49$	900.341	332.977	3.26e-14	yes
$^{28}Si^{32}S$	$v = 1–1$, $J = 51–50$	918.224	326.491	3.48e-14	no
$^{28}Si^{32}S$	$v = 1–1$, $J = 52–51$	936.101	320.257	3.69e-14	no
$^{28}Si^{32}S$	$v = 1–1$, $J = 53–52$	953.970	314.258	3.89e-14	yes
$^{28}Si^{32}S$	$v = 1–1$, $J = 54–53$	971.831	308.482	4.08e-14	yes

Table A.1. continued.

Molecule	Transition	Frequency [GHz]	Wavelength [μm]	Integrated Flux [erg/cm^2/s]	Blend
^{28}Si^{32}S	v = 1−1, J = 55−54	989.685	302.917	4.28e-14	yes
^{28}Si^{32}S	v = 1−1, J = 56−55	1007.530	297.552	4.47e-14	no
^{28}Si^{32}S	v = 1−1, J = 57−56	1025.368	292.376	4.67e-14	yes
^{28}Si^{32}S	v = 1−1, J = 58−57	1043.197	287.378	4.86e-14	no
^{28}Si^{32}S	v = 1−1, J = 59−58	1061.018	282.552	5.03e-14	yes
^{28}Si^{32}S	v = 1−1, J = 60−59	1078.831	277.886	5.21e-14	yes
^{28}Si^{32}S	v = 1−1, J = 61−60	1096.635	273.375	5.37e-14	yes
^{28}Si^{32}S	v = 1−1, J = 62−61	1114.430	269.010	5.51e-14	yes
^{28}Si^{32}S	v = 1−1, J = 63−62	1132.217	264.784	5.61e-14	yes
^{28}Si^{32}S	v = 1−1, J = 64−63	1149.994	260.690	5.68e-14	yes
^{28}Si^{32}S	v = 1−1, J = 65−64	1167.763	256.724	5.84e-14	yes
^{28}Si^{32}S	v = 1−1, J = 66−65	1185.522	252.878	6.09e-14	yes
^{28}Si^{32}S	v = 1−1, J = 67−66	1203.271	249.148	6.29e-14	yes
^{28}Si^{32}S	v = 1−1, J = 68−67	1221.011	245.528	6.42e-14	yes
^{28}Si^{32}S	v = 1−1, J = 69−68	1238.741	242.014	6.46e-14	yes
^{28}Si^{32}S	v = 1−1, J = 70−69	1256.461	238.601	6.40e-14	yes
^{28}Si^{32}S	v = 1−1, J = 71−70	1274.171	235.284	6.70e-14	no
^{28}Si^{32}S	v = 1−1, J = 72−71	1291.871	232.061	6.87e-14	yes
^{28}Si^{32}S	v = 1−1, J = 73−72	1309.561	228.926	6.86e-14	yes
^{28}Si^{32}S	v = 1−1, J = 74−73	1327.240	225.877	6.86e-14	yes
^{28}Si^{32}S	v = 1−1, J = 75−74	1344.908	222.909	7.11e-14	yes
^{28}Si^{32}S	v = 1−1, J = 76−75	1362.566	220.021	1.68e-14	no
^{28}Si^{32}S	v = 1−1, J = 77−76	1380.213	217.207	1.84e-14	yes
^{28}Si^{32}S	v = 1−1, J = 78−77	1397.849	214.467	2.06e-14	yes
^{28}Si^{32}S	v = 1−1, J = 79−78	1415.473	211.797	2.16e-14	yes
^{28}Si^{32}S	v = 1−1, J = 80−79	1433.086	209.194	7.36e-14	yes
^{28}Si^{32}S	v = 1−1, J = 81−80	1450.688	206.655	2.50e-14	no
^{28}Si^{32}S	v = 1−1, J = 82−81	1468.278	204.180	2.65e-14	yes
^{28}Si^{32}S	v = 1−1, J = 83−82	1485.857	201.764	2.78e-14	yes
^{28}Si^{32}S	v = 1−1, J = 84−83	1503.423	199.407	2.93e-14	yes
^{28}Si^{32}S	v = 1−1, J = 85−84	1520.978	197.105	7.32e-14	yes
^{28}Si^{32}S	v = 1−1, J = 86−85	1538.520	194.858	3.18e-14	yes
^{28}Si^{32}S	v = 1−1, J = 87−86	1556.050	192.662	3.18e-14	no
^{28}Si^{32}S	v = 1−1, J = 88−87	1573.567	190.518	7.40e-14	no
^{28}Si^{32}S	v = 1−1, J = 89−88	1591.072	188.422	7.36e-14	yes
^{28}Si^{32}S	v = 1−1, J = 90−89	1608.564	186.373	7.34e-14	no
^{28}Si^{32}S	v = 1−1, J = 91−90	1626.043	184.369	7.26e-14	no
^{28}Si^{32}S	v = 1−1, J = 92−91	1643.509	182.410	7.13e-14	yes
^{28}Si^{32}S	v = 1−1, J = 93−92	1660.962	180.493	7.07e-14	yes
^{28}Si^{32}S	v = 1−1, J = 94−93	1678.402	178.618	7.18e-14	no
^{28}Si^{32}S	v = 1−1, J = 95−94	1695.828	176.782	6.93e-14	no
^{28}Si^{32}S	v = 1−1, J = 96−95	1713.240	174.986	6.97e-14	no
^{28}Si^{32}S	v = 1−1, J = 97−96	1730.639	173.226	6.67e-14	yes
^{28}Si^{32}S	v = 1−1, J = 98−97	1748.024	171.504	6.84e-14	no
^{28}Si^{32}S	v = 1−1, J = 99−98	1765.394	169.816	6.79e-14	yes
^{28}Si^{32}S	v = 1−1, J = 100−99	1782.751	168.163	6.66e-14	yes
^{28}Si^{32}S	v = 1−1, J = 101−100	1800.093	166.543	6.38e-14	no
^{28}Si^{32}S	v = 1−1, J = 102−101	1817.420	164.955	6.52e-14	no
^{28}Si^{32}S	v = 1−1, J = 103−102	1834.733	163.398	6.21e-14	no
^{28}Si^{32}S	v = 1−1, J = 104−103	1852.032	161.872	6.32e-14	yes
^{28}Si^{32}S	v = 1−1, J = 105−104	1869.315	160.376	6.08e-14	yes
^{28}Si^{32}S	v = 1−1, J = 106−105	1886.583	158.908	6.00e-14	yes
^{28}Si^{32}S	v = 1−1, J = 107−106	1903.836	157.468	6.00e-14	yes
^{28}Si^{32}S	v = 1−1, J = 108−107	1921.074	156.055	5.87e-14	yes
^{28}Si^{32}S	v = 1−1, J = 109−108	1938.296	154.668	5.77e-14	yes

Notes. The integrated flux values in the fifth column are for the model predictions as shown in Fig. 1. The last column indicates whether a line is blended strongly with another line.